

Determining Tropical Cyclone Surface Wind Speed Structure and Intensity with the CYGNSS Satellite Constellation

MARY MORRIS^a AND CHRISTOPHER S. RUF

Department of Climate and Space Sciences and Engineering, University of Michigan, Ann Arbor, Michigan

(Manuscript received 30 November 2016, in final form 18 April 2017)

ABSTRACT

The Cyclone Global Navigation Satellite System (CYGNSS) consists of a constellation of eight microsatellites that provide observations of surface wind speed in all precipitating conditions. A method for estimating tropical cyclone (TC) metrics—maximum surface wind speed V_{MAX} , radius of maximum surface wind speed R_{MAX} , and wind radii (R_{64} , R_{50} , and R_{34})—from CYGNSS observations is developed and tested using simulated CYGNSS observations with realistic measurement errors. Using two inputs, 1) CYGNSS observations and 2) the storm center location, estimates of TC metrics are possible through the use of a parametric wind model algorithm that effectively interpolates between the available observations as a constraint on the assumed wind speed distribution. This methodology has a promising performance as evaluated from the simulations presented. In particular, after quality-control filters based on sampling properties are applied to the population of test cases, the standard deviation of retrieval error for V_{MAX} is 4.3 m s^{-1} (where $1 \text{ m s}^{-1} = 1.94 \text{ kt}$), for R_{MAX} is 17.4 km, for R_{64} is 16.8 km, for R_{50} is 21.6 km, and for R_{34} is 41.3 km (where $1 \text{ km} = 0.54 \text{ n mi}$). These TC data products will be available for the 2017 Atlantic Ocean hurricane season using on-orbit CYGNSS observations, but near-real-time operations are the subject of future work. Future work will also include calibration and validation of the algorithm once real CYGNSS data are available.

1. Introduction

a. Motivation

Tropical cyclones (TCs) and their precursor storms spend most—if not all—of their lifetimes over the ocean, which makes them harder to observe in situ. Since the advent of remote sensing, fewer TCs go unobserved (Vecchi and Knutson 2011), and our increased observation of these storms has led to improved understanding of TC processes. Additionally, the observations that are collected through remote sensing support the TC situational awareness and forecasting efforts at warning centers like the National Hurricane Center (NHC) (Rappaport et al. 2009).

Forecasters are required to estimate the present and predict the future intensity of TCs, typically defined

as the maximum 1- or 10-min sustained wind speed at the 10-m observing level associated with the system (Harper et al. 2010; Office of the Federal Coordinator for Meteorological Services and Supporting Research 2017). Only 30% of the 6-hourly intensity estimates in the North Atlantic Ocean (Rappaport et al. 2009) are guided by aircraft reconnaissance, and next to no aircraft reconnaissance is performed elsewhere. Unfortunately, accurate intensity estimation remains challenging with and without aircraft reconnaissance. Intensity estimates in the postseason reanalysis records have uncertainties of approximately 5 m s^{-1} (Landsea and Franklin 2013; Torn and Snyder 2012). Often, the observational guidance that TC forecasters use is based entirely on remote sensing observations.

Observations of surface wind speed can inform estimates of the intensity of a system. In addition to intensity estimation, surface wind speed observations can also guide forecasters who are analyzing the maximum radial extent of 34-, 50-, and 64-kt ($1 \text{ kt} = 0.51 \text{ m s}^{-1}$) surface winds from the center of a storm in geographic quadrants—commonly collectively referred to as wind

^a Current affiliation: Jet Propulsion Laboratory, Pasadena, California.

Corresponding author: Mary Morris, mary.g.morris@jpl.nasa.gov

radii. Wind radii give insight into the surface wind structure and therefore are useful for a variety of applications (Knaff et al. 2016).

b. Examples of previous efforts

Satellite remote sensing-based methods have been developed to estimate intensity in situations where aircraft reconnaissance is not available. One of these methods is the Dvorak technique: a method of estimating TC intensity through image pattern recognition. Two types of Dvorak techniques exist: subjective and objective.

The subjective Dvorak methods were first based on visible imagery from geostationary meteorological satellites (Dvorak 1975); infrared imagery is now included in the technique (Dvorak 1984). The subjective Dvorak technique has proven to be a useful tool for estimating intensity operationally. A discussion of known performance limitations and error characteristics can be found in Knaff et al. (2010).

To lessen subjectivity and increase automation, objective Dvorak methods have been developed (Velden et al. 2006), leading to the objective Dvorak technique (ODT) (Velden et al. 1998) and, more recently, the advanced Dvorak technique (ADT) (Olander and Velden 2007). Dvorak techniques rely on data from geostationary satellites and are not plagued by data gaps typically seen if relying on polar-orbiting satellites or aircraft reconnaissance alone.

Because of the usefulness of geostationary data availability, a variety of other methods for TC characterization—both intensity and wind structure estimation—have been developed for geostationary infrared imagery and data (e.g., Mueller et al. 2006; Kossin et al. 2007; Piñeros et al. 2008, 2011; Fetanat et al. 2013; Knaff et al. 2015; Dolling et al. 2016). A number of studies have developed methods that need an estimate of storm intensity in order to estimate wind structure from infrared data (Mueller et al. 2006; Kossin et al. 2007; Knaff et al. 2011, 2015). The deviation angle variance (DAV) technique developed by Piñeros et al. (2008, 2011) correlates intensity and structure with the gradient in infrared brightness temperature; the DAV-based wind radii methods presented in Dolling et al. (2016) use a multiple linear regression technique. Fetanat et al. (2013) take advantage of historical hurricane satellite data (HURSAT) to estimate intensity from feature analogs—or brightness temperature patterns—in satellite imagery and analogous storms. In addition to infrared data inputs, the methods developed in Knaff et al. (2011, 2015) take advantage of multiple satellite inputs to estimate the TC wind field, from which wind radii are estimated.

TC intensity estimation is also possible using passive microwave sounders, like AMSU. This method takes advantage of the correlation between a TC's warm-core structure and its intensity. Warm-core anomalies are greatest during peak intensity. Using the retrieved vertical temperature structure from AMSU, estimates of the minimum surface level pressure and maximum sustained wind speed are possible through the hydrostatic approximation and assumptions of gradient wind balance (Kidder et al. 2000). Care has to be taken to account for the effect of clouds and precipitation on the AMSU radiances. While AMSU does not have adequate horizontal resolution to estimate realistic wind structure alone, estimates of the 34-, 50-, and 64-kt wind radii and maximum wind speed can be made using statistically based algorithms (Bessho et al. 2006; Demuth et al. 2006). The performance from this microwave-sounder-type method is comparable to the Dvorak technique, but since this method relies on polar-orbiting sounders, temporal sampling of the TC inner core is limited.

Knaff et al. (2016) developed methods for estimating wind radii using routinely available estimates of TC intensity, motion, and location. These inputs, together with estimates of TC size from IR imagery or model analyses, are used to create modified Rankine vortices—one for each wind threshold—from which wind radii are estimated.

Scatterometers are used to measure ocean vector winds and therefore have some utility in observing TC scenes. Some examples of spaceborne scatterometers include the Ku-band NASA Quick Scatterometer (QuikScat) (Ebuchi et al. 2002), its replacement Rapid Scatterometer (RapidScat) (Madsen and Long 2016), which was put onboard the International Space Station, and the ESA/EUMETSAT series of C-band Advanced Scatterometers (ASCATs) (Figa-Saldana et al. 2002). A more complete discussion of the limitations of scatterometer observations of TC scenes is contained in Brennan et al. (2009). Most notably, scatterometers lose sensitivity at high wind speeds and are often plagued by rain contamination. However, scatterometer observations are valuable for wind radii analyses, with good reliability for 34-kt radius estimation.

L-band radiometers also have applications in observing storms. Observations from the Soil Moisture Active Passive (SMAP) (Fore et al. 2016) and the Soil Moisture Ocean Salinity (SMOS) (Reul et al. 2012, 2016) missions are useful for TC applications because the low-frequency observations are uncontaminated by rain. However, the spatial resolution of these instruments limits their performance. For example, SMAP

observations, with a resolution of 60 km, require additional scaling if intensity is to be estimated from them. Yueh et al. (2016) developed SMAP-based TC intensity estimation methods after relating the V_{MAX} observed by the SMAP platform to the true V_{MAX} . Unfortunately, polar-orbiting satellites like these have poor revisit times.

c. CYGNSS

The Cyclone Global Navigation Satellite System (CYGNSS) constellation of eight small satellites provides unique ocean surface wind speed observations in all precipitating conditions (Ruf et al. 2016). The retrieval uncertainty is anticipated to be 2 m s^{-1} for winds less than 20 m s^{-1} and 10% for winds greater than 20 m s^{-1} . Like SMAP/SMOS, CYGNSS operates at a sufficiently low frequency to see through the high precipitation of a TC eyewall and observe the highest surface wind speeds of TCs. Each CYGNSS observatory has a four-channel bistatic radar receiver for measuring the GPS L1 (1.575 GHz) signal reflected from the surface of Earth. Unlike SMAP/SMOS, CYGNSS observations will be $25 \times 25 \text{ km}^2$. Its temporal sampling is also significantly more frequent. Using a constellation of eight satellites in low-inclination circular orbit allows for mean and median revisit times over the tropics of 7.2 and 2.8 h, respectively.

While CYGNSS observations will be useful for estimating TC intensity and wind structure, there are some challenges to overcome with this new observing system. The sampling patterns are not analogous to the continuous-swath observations typical of other spaceborne wind-sensing instruments (e.g., SMAP, SMOS, and ASCAT). CYGNSS observes winds along a series of narrow tracks through the storm; portions of the wind field between observation tracks are not directly sampled. If for example, a CYGNSS-based intensity estimation method involved simply finding the highest wind speed observed by CYGNSS through a storm, the intensity estimate might not have good performance if the gaps in sampling happened to coincide with the location of maximum winds.

If the CYGNSS mission successfully demonstrates the value of its data products, a transition to near-real-time operations is possible in the future, and the data products developed here could be available to operational agencies. However, it should be noted that there are currently no plans for real-time data processing.

d. Outline

The capabilities of CYGNSS have wide applicability to TC science and forecasting activities. In this paper,

CYGNSS-based methods are developed for the estimation of a variety of metrics commonly used to describe TCs: intensity (based on V_{MAX}), the radius of maximum winds R_{MAX} , and wind radii (R_{34} , R_{50} , and R_{64} , corresponding to the 34-, 50-, and 64-kt wind radii, respectively). Section 2 describes the datasets used to develop and evaluate the method. Section 3 describes the algorithm. Sections 4 and 5 characterize the performance of the CYGNSS-based estimates of intensity and wind structure and develop quality-control measures of its reliability. Section 6 discusses these results. Section 7 offers some conclusions and opportunities for future investigations.

2. Datasets

A large set of realistic simulated observations was created using the CYGNSS end-to-end simulator (E2ES) (O'Brien 2014) in order to develop and test the CYGNSS integrated kinetic energy (IKE) algorithm prior to launch. The E2ES generates simulated CYGNSS level 2 wind speed data products from a time-evolving input wind field. It properly accounts for both the spatial and temporal peculiarities of the CYGNSS measurement technique by forward propagating the orbital trajectories of every satellite in the GPS and CYGNSS constellations and computing the location of the specular reflection point on Earth's surface as a function of time for every possible GPS/CYGNSS pair. Additionally, the E2ES properly accounts for the 25-km spatial resolution of the CYGNSS wind speed measurements by appropriately averaging the input wind field, and it accounts for its measurement uncertainty by corrupting the input "truth" winds with noise that is statistically representative of the expected precision of the level 2 wind speed retrieval algorithm (Clarizia and Ruf 2016).

Simulated CYGNSS observations were generated using real-time wind field analyses and forecasts produced by the operational version of the Hurricane Weather Research and Forecasting (HWRF) Model (Tallapragada et al. 2013) for Atlantic and Pacific Ocean storms during 2010, 2011, 2013, and 2014. HWRF wind fields were generated for storms every 3 h throughout their life cycles; 0300, 0900, 1500, and 2100 UTC data are the 3-h forecast fields for the previous analysis time. From each 3-h snapshot from HWRF, CYGNSS observations were simulated.

After the simulation data were created, a number of quality-control (QC) metrics were applied in order to get the best population of test cases to effectively test the methods presented in this paper. For each test case, there had to be no land in the smallest

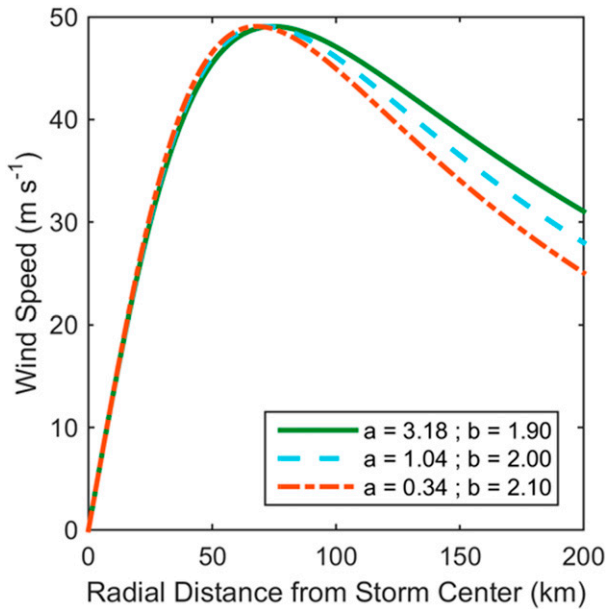


FIG. 1. An example of the wind speed relationship from the parametric model in Eq. (2) with three different “ b ” parameters used; $V_{m,p} = 50 \text{ m s}^{-1}$, $R_{m,p} = 75 \text{ km}$, and the center position latitude is 15° .

HWRf domain, a maximum wind speed of at least 17.49 m s^{-1} was required, and the center position—provided by the best-track databases (Chu et al. 2002; Landsea and Franklin 2013)—had to be within 1° latitude and longitude of the center of the smallest HWRf domain.

Performance of the algorithm is characterized using comparisons with simulated truth values derived from the HWRf data. True V_{MAX} is defined as the maximum surface wind speed in the smallest HWRf domain. True R_{MAX} is determined from the average location of the winds falling above the 95th percentile in the smallest HWRf domain. The true wind radii are determined from the extent of certain strengths (34, 50, and 64 kt) of wind speed within the smallest HWRf domain. In addition to the previously mentioned QC, cases for which the true R_{34} was located at the edge of the smallest HWRf domain were also excluded. After all QC filters are applied, a total of 302 test cases remain for developing and testing the algorithm in this study (details of each case are given in Table A1 in appendix A). A wide variety of storms are included. There are 113 cases from the Atlantic and eastern Pacific. There are 189 cases from the western Pacific. The mean R_{34} across all cases is 248 km, with a standard deviation of 99 km. The highest intensity (74 m s^{-1}) test cases are found in the Lekima (2013) and Vongfong (2014) storms.

3. Methodology

a. Parametric wind model

CYGNSS wind speed observation tracks often have large gaps between them—gaps that may be in areas of interest (e.g., the location of the maximum wind speed). To account for the areas that have been missed by CYGNSS, a method is developed that effectively interpolates between the available observations using a parametric model as a constraint on the assumed wind speed distribution.

The parametric wind model used has roots in the method developed in Emanuel and Rotunno (2011) and was used in a previous study by Morris and Ruf (2017). In Emanuel and Rotunno (2011), the parametric wind profile most applicable to the region inside of approximately $2.5R_{MAX}$ is given by

$$V(r) = \frac{2r \left(R_{m,p} V_{m,p} + \frac{1}{2} f R_{m,p}^2 \right)}{R_{m,p}^2 + r^2} - \frac{fr}{2}, \quad (1)$$

where $R_{m,p}$ is the radius of maximum winds, $V_{m,p}$ is the maximum wind speed, r is the radial distance from the storm center, and f is the Coriolis parameter. The Coriolis parameter is determined by the storm center location coordinates and is not an independent parameter to be estimated from the CYGNSS observations.

As discussed in Chavas et al. (2015), the outer wind radii tend to be underestimated by Eq. (1). To address this tendency, two additional parameters have been added to the model to regulate the rate of decay of the wind speed at large radii. The model is given by

$$V(r) = \frac{2r \left(R_{m,p} V_{m,p} + \frac{1}{2} f R_{m,p}^2 \right)}{R_{m,p}^2 + ar^b} - \frac{fr}{2}, \quad (2)$$

where the two additional parameters are a and b . Examples of the wind speed radial dependence specified by Eq. (2) are shown in Fig. 1.

Of the four model parameters— $R_{m,p}$, $V_{m,p}$, a , and b — a can be solved from the other three by requiring that the maximum value of $V(r)$ be equal to the parameter $V_{m,p}$. The solution for a is outlined in appendix B. This effectively reduces Eq. (2) to a three-parameter model. As shown in Fig. 1, the b parameter allows for adjustment of the radial decay rate of the wind speed in the outer storm region. Larger values of b correspond to a faster radial decay. The model is fit to the CYGNSS wind speed data by adjusting the three parameters, $R_{m,p}$, $V_{m,p}$, and b , to minimize the sum-squared difference

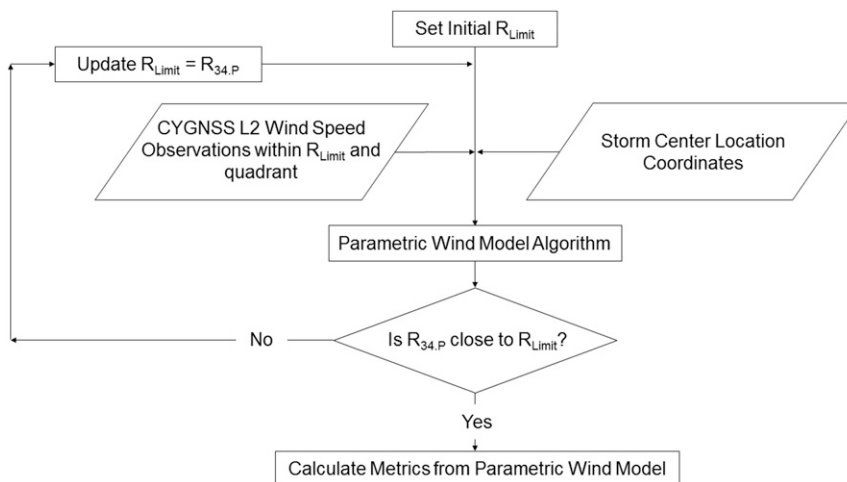


FIG. 2. A flow diagram that outlines the steps of the CYGNSS TC surface wind speed structure and intensity product algorithms.

between the model and all CYGNSS observations within a specified region near the storm center.

b. Parametric retrieval algorithm

A flow diagram of the parametric model retrieval algorithm is shown in Fig. 2. First, depending on the basin in question, an initial R_{Limit} —the maximum radial distance from the storm center over which to draw an initial set of CYGNSS observations from—is set. For the Atlantic and eastern Pacific storms, the initial $R_{Limit} = 200$ km. For the western Pacific storms, the initial $R_{Limit} = 300$ km, as these storms are generally larger (Chan and Chan 2012; Chavas and Emanuel 2010; Knaff et al. 2014; Sampson et al. 2016). The algorithm requires two sets of inputs: 1) CYGNSS observations and 2) the center position of the storm. The amount of CYGNSS observation input also depends on the type of metric being estimated. For the wind radii estimates, which are quadrant dependent, only observations within a particular quadrant are used. If no observations are available in a quadrant, wind radii are not estimated there. However, observations available across the entire storm are used for estimates of V_{MAX} and R_{MAX} .

Once the initial set of CYGNSS wind speed data is gathered, it is input into the parametric wind model algorithm. In this algorithm, the free parameters $R_{m,p}$, $V_{m,p}$, and b are solved using an iterative least squares estimator. The procedures behind the parametric wind model algorithm are outlined in appendix C. These estimates are used to create a best-fit parametric wind model to the available observations. An example of this process is shown in Fig. 3. In Fig. 3a, the HWRP wind field from which the CYGNSS observations are derived

is shown. In Fig. 3b, the simulated CYGNSS observations are shown for this test case. In Fig. 3c, an example of the final best-fit parametric wind model over all quadrants is shown. The model effectively interpolates between the gaps in the track, which are shown in Fig. 3b. The parametric model is used to derive V_{MAX} and R_{MAX} .

Figure 3c also highlights another aspect of the algorithm flow shown in Fig. 2. Initially, observations within 300 km of the storm center are used. However, after the initial run of the algorithm, if the estimate of $R_{34,P}$ (the parametric model estimate of R_{34}) is different than 300 km, then the algorithm is repeated until R_{Limit} and $R_{34,P}$ converge. In the test case shown in Fig. 3, fewer observations are used in the final iteration of the algorithm because the final value of R_{Limit} after convergence is less than 300 km.

Once the best-fit parametric model solution is attained, the metrics of interest can be derived from it. The parametric V_{MAX} is defined as the maximum of $V(r)$ and the parametric R_{MAX} is defined as that r where the parametric V_{MAX} occurs. The parametric wind radii are defined by the radius at the wind strength in question in the parametric model.

c. Three- versus two-parameter model impacts

In Fig. 4, the parametric model algorithm process is examined for a particular northeast quadrant test case. In this example, however, the results from using the two-parameter model given by Eq. (1) are shown in addition to those from using the three-parameter model [Eq. (2)]. In this test case, the simulated CYGNSS observations suggest that the decay in wind speed is slower than the original two-parameter model would fit. The estimates

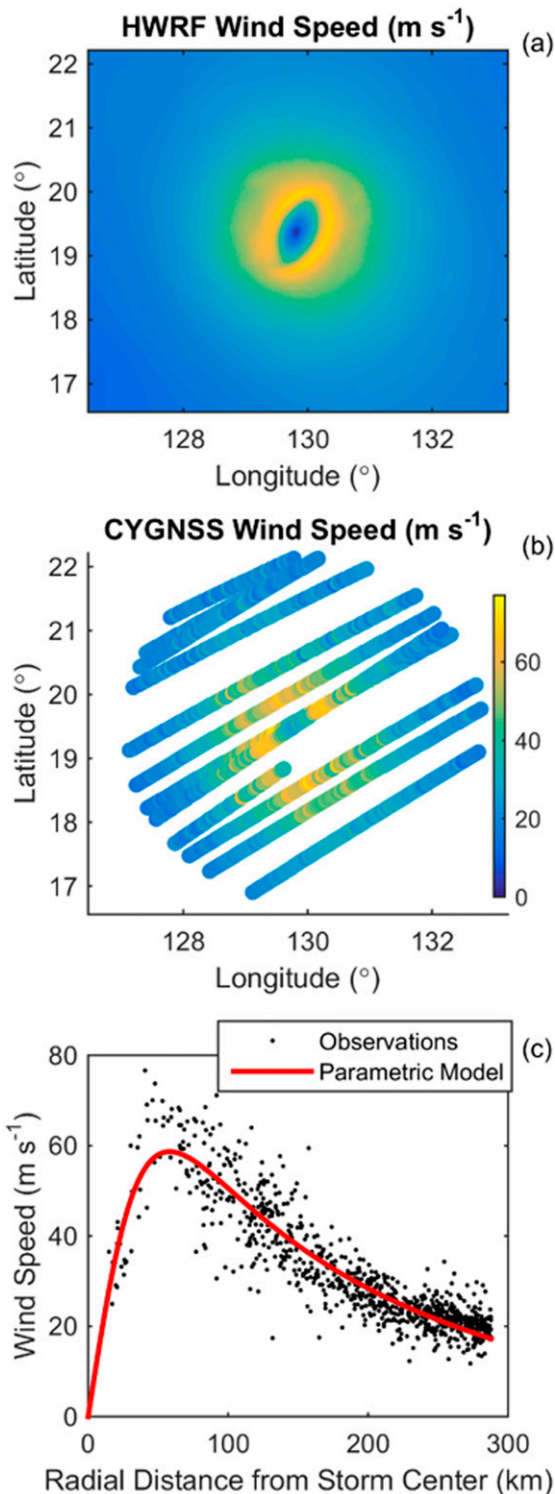


FIG. 3. (a) HWRP wind speed field for Vongfong at 0300 UTC 9 Oct 2014, (b) simulated CYGNSS wind speed observations for (a), and (c) the parametric model algorithm fit for this test case.

of the outer wind radii are improved by use of a model with a more flexible radial decay.

d. Parametric scaling

There are two main drivers for this algorithm design: measurement noise and variable coverage. The variable nature of coverage from the CYGNSS constellation means that sometimes the maximum winds are not sampled directly. The use of a parametric wind model helps to overcome these two factors. However, after the model is fit to the available observations, parametric scaling—developed below—is needed to determine the final metrics. For a number of reasons, estimates of the intensity, radius of maximum wind, and wind radii derived directly from the parametric model function $V(r)$ are found to have characteristic scale and bias difference from the actual values. This is true whether the parametric model is derived only from CYGNSS observations or is fit to the complete grid of HWRP wind samples. To elaborate further on this, even if perfect noise-free observations existed, the lowest observations would balance the highest ones, creating a bias in estimates derived directly from the best-fit parametric model. Another bias-inducing factor to consider is that CYGNSS data, at 25-km resolution, spatially filter some TC features. Scaling factors derived here help to correct for the characteristic bias and scale differences caused by these spatial filter–related factors as well as overcome limitations from using a simple parametric model.

The scale and bias differences are compensated by scaling the values derived directly from the parametric model using a power series transformation. The coefficients in the power series are determined as follows: Best-fit parametric models are determined for all storm cases using the complete grid of HWRP wind samples. In each case, estimates of the intensity $V_{\max,p}$, radius of maximum wind $R_{\max,p}$, and wind radii ($R_{34,p}$, $R_{50,p}$, and $R_{64,p}$) are derived directly from the parametric model and compared with the true values determined from the actual HWRP winds. A power series is fit to the comparison that translates the direct parametric values to scaled values that are closest, in a least squares sense, to the true values. A first-order power series is found to be sufficient for scaling the intensity and the three wind radii estimates, and a third-order power series is found to be necessary for scaling the estimate of the radius of maximum wind. The scaling relationships have the form

$$V_{\max,\text{scaled-p}} = a_0 + a_1 V_{\max,p}, \quad (3a)$$

$$R_{\max,\text{scaled-p}} = a_0 + a_1 R_{\max,p} + a_2 R_{\max,p}^2 + a_3 R_{\max,p}^3, \quad (3b)$$

$$R_{34,\text{scaled-p}} = a_0 + a_1 R_{34,p}, \quad (3c)$$

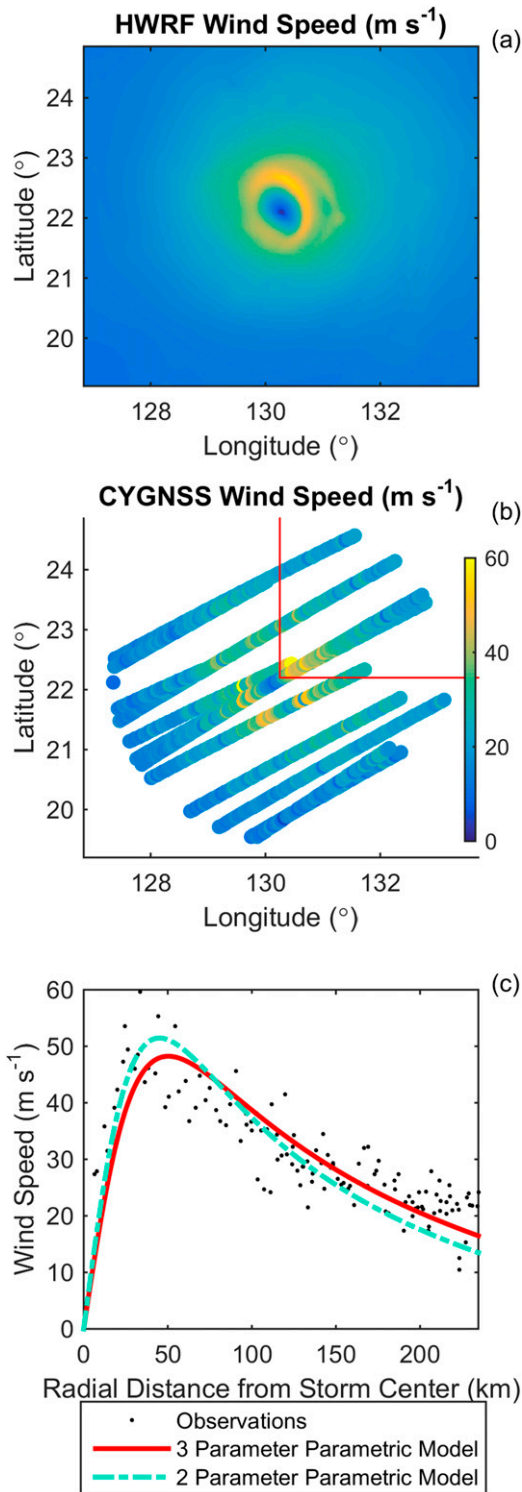


FIG. 4. (a) HWRP wind speed field for Soulik at 0300 UTC 11 Jul 2013, (b) simulated CYGNSS wind speed observations for (a) with the NE quadrant (cornered off by red lines) currently being considered, and (c) the parametric model algorithm fit for this NE quadrant test case from which the NE quadrant wind radii are solved.

TABLE 1. Coefficients used for translation from the parametric metrics to the scaled-parametric metrics, assuming the form of Eq. (3).

Metric	a_0	a_1	a_2	a_3
V_{MAX} ($m s^{-1}$)	5.605 266	1.131 274	0	0
R_{MAX} (km)	51.951 488	0.228 911	0.003 682	-0.000 006
R_{34} (km)	42.564 232	1.098 006	0	0
R_{50} (km)	11.904 758	1.006 752	0	0
R_{64} (km)	9.444 089	0.975 245	0	0

$$R_{50.max.scaled-p} = a_0 + a_1 R_{50.p}, \quad \text{and} \quad (3d)$$

$$R_{64.max.scaled-p} = a_0 + a_1 R_{64.p}. \quad (3e)$$

The coefficients used in this study are given in Table 1. In summary, TC metrics are first derived directly from the best-fit parametric model. The metrics derived directly from the best-fit parametric model are more representative of the mean value of those metrics. So, for example, the wind radii derived from the parametric model represent something closer to a mean extent rather than the maximum extent (i.e., the operational metric). To estimate the maximum extent, Eqs. (3c)–(3e) are applied. All metrics are corrected using Eqs. (3) and the coefficients in Table 1 to estimate the true TC metrics. These final estimates will henceforth be referred to as the scaled-parametric metrics.

4. Initial results

a. Performance without quality control

To illustrate the effect of applying the scaling factors described above, histograms of error are plotted in Fig. 5 for each of the TC metrics. These histograms include all storm cases, with no QC filters related to algorithm performance applied. Both the parametric and scaled-parametric metrics are plotted to show that the scaling alleviates some of the larger biases in the parametric estimates. For example, there is a clear overall bias in the parametric V_{MAX} , but after the scaling correction is applied, the mean error is close to zero. The mean and standard deviation of each population of errors are reported in Table 2. For some metrics, the scaling factor improves performance much more than for others. The inner wind radii R_{50} and R_{64} have very small scaling factors; their performance improves by a small amount. The standard deviations reported in Table 2 show that R_{MAX} is the only metric where the scaling factors affect the root-mean-square error (RMSE) by a significant amount. The RMSE can be further improved by applying QC filters. These filters are developed below.

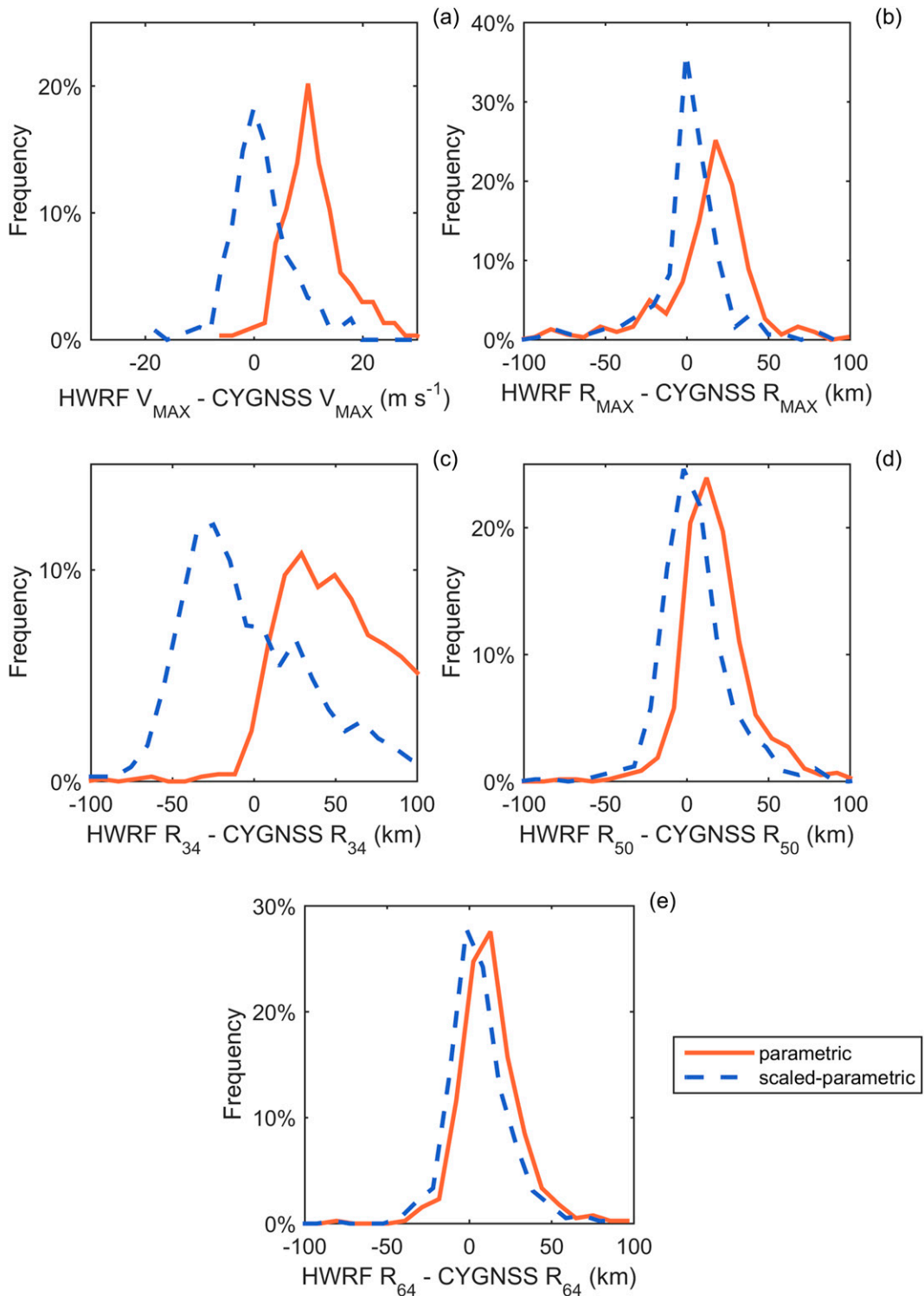


FIG. 5. Histograms of error, normalized to percentages, before QC is applied in all parametric and scaled-parametric metrics. Error is defined here as true – estimated.

TABLE 2. Mean and standard deviation of the error plotted in Fig. 5 for each parametric and scaled-parametric metric.

Metric	Mean		Standard deviation	
	Parametric	Scaled parametric	Parametric	Scaled parametric
V_{MAX} ($m s^{-1}$)	10.4	0.8	6.9	7.2
R_{MAX} (km)	1.7	-6.4	54.0	41.7
R_{34} (km)	57.4	-5.9	55.6	57.3
R_{50} (km)	11.9	-1.1	33.4	33.5
R_{64} (km)	5.7	-0.6	27.7	27.2

b. Sensitivity to storm center location error

One of the required inputs to the TC metric estimator algorithm is the location of the storm center. During algorithm development, the best-track database is used for storm center information, and storm center data sources have yet to be finalized for on-orbit data processing. Potential sources of center information include the working best track, interpolation from the forecast track or an objective position location algorithm such as that from the Automated Rotational Center Hurricane Eye Retrieval (ARCHER) (Wimmers and Velden 2010).

Sensitivity experiments were performed to assess the impact of center location error on the metrics. In these experiments, the algorithm was executed multiple times using all available test cases, each time perturbing the center position latitude by an increasing amount. After performing some quality control (described in the following section), the error due to latitude offset was calculated by decomposing it from the overall error in the TC metric estimate. Specifically, the RMSE due to center location offset is given by

$$RMSE_{off}(x) = \sqrt{RMSE_{total}(x)^2 - RMSE_{off,x=0}^2}, \quad (4)$$

where $RMSE_{total}$ is the total RMSE for a certain offset x , and $RMSE_{off,x=0}$ is the RMSE with no latitude offset. The results are shown in Fig. 6 for V_{MAX} and R_{MAX} , the metrics that are derived using observations from all four quadrants, and in Fig. 7 for wind radii, the metrics derived in individual quadrants. For the wind radii, the northeast quadrant was used. The results are similar in other quadrants.

The results show a consistent monotonic increase in error with increasing uncertainty in the storm center location for all TC metrics. For example, a storm center offset of 55 km introduces an RMSE in V_{MAX} of $4.7 m s^{-1}$; in R_{MAX} of 12 km; and in R_{64} , R_{50} , and R_{34} of 39, 43, and 48 km, respectively. In terms of relative error (relative to the mean value of each TC metric), these errors correspond to 12% for V_{MAX} ; 13% for R_{MAX} ; and 32%, 28%, and 19% for R_{64} , R_{50} , and R_{34} .

c. Sensitivity to CYGNSS coverage

The spatial distribution of observations, or coverage, by CYGNSS of the TC wind field will affect the quality of its retrieval of the TC metrics. The sensitivity of the retrievals to coverage is illustrated in Figs. 8 and 9.

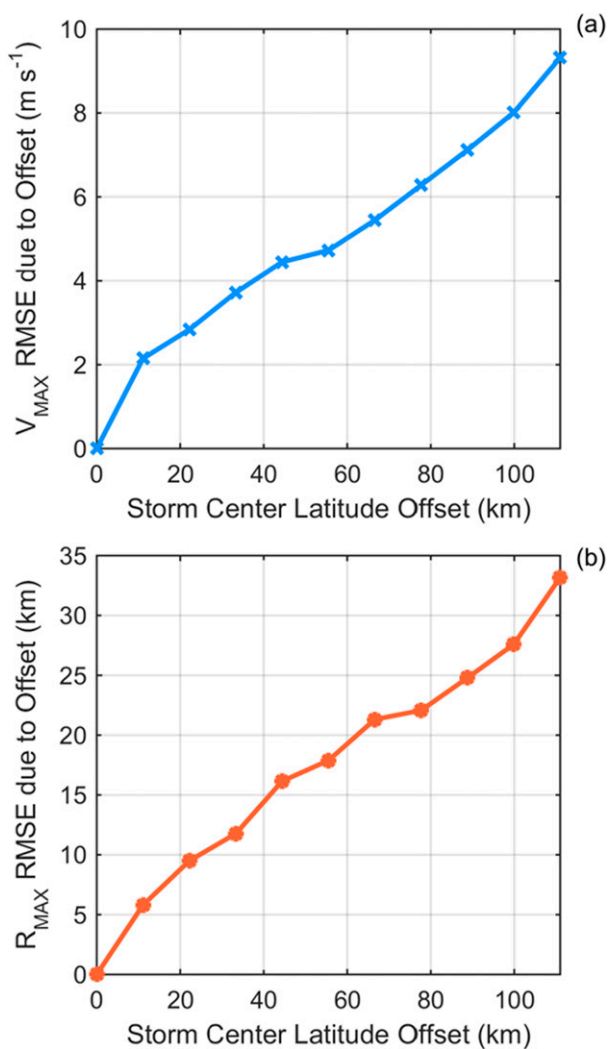


FIG. 6. The additional error on average to expect from storm center offsets (here, only in latitude) for (a) V_{MAX} and (b) R_{MAX} .

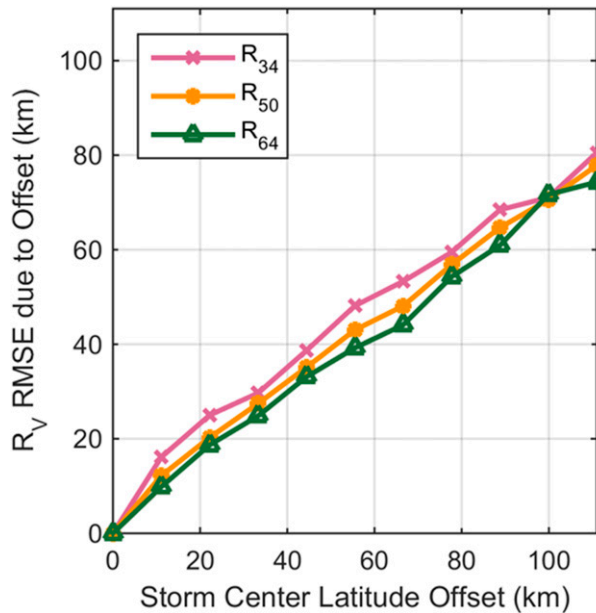


FIG. 7. The additional error on average to expect from storm center offsets (here, only in latitude) for wind radii. This analysis is based on the cases available in the NE quadrant.

Different sampling characteristics are considered and different regions are examined for different TC metrics. Figure 8 shows the sensitivity of V_{MAX} (Fig. 8a) and R_{MAX} (Fig. 8b) performance to the number of CYGNSS samples, or observations, within 100 km of the storm center. Other thresholds were examined, and 100 km provided the best sensitivity for V_{MAX} and R_{MAX} . In Fig. 8, the root-mean-square difference (RMSD) between the HWRf and CYGNSS values is shown for different populations of storm cases. The population used for the RMSD calculation is selected based on the coverage threshold attained (defined on the x axis), or the number of observations within 100 km of the storm center in a test case. The x axis in the figure is the threshold—the (minimum) number of observations required within 100 km. For example, at an x -axis value of 10, the population of test cases that went into the RMSD calculation at this point all had at least 10 CYGNSS observations within 100 km of the storm center. Cases with poor coverage near the center of the storm drive the RMSD up; these cases are included in the population at low sample number thresholds. As the threshold is increased, more and more undersampled cases are thrown out, and the performance improves. The key takeaway from these results is that an adequate number of CYGNSS observations are needed within the inner core in order to make a reliable estimate of inner-core metrics like V_{MAX} and R_{MAX} . Therefore, quality control

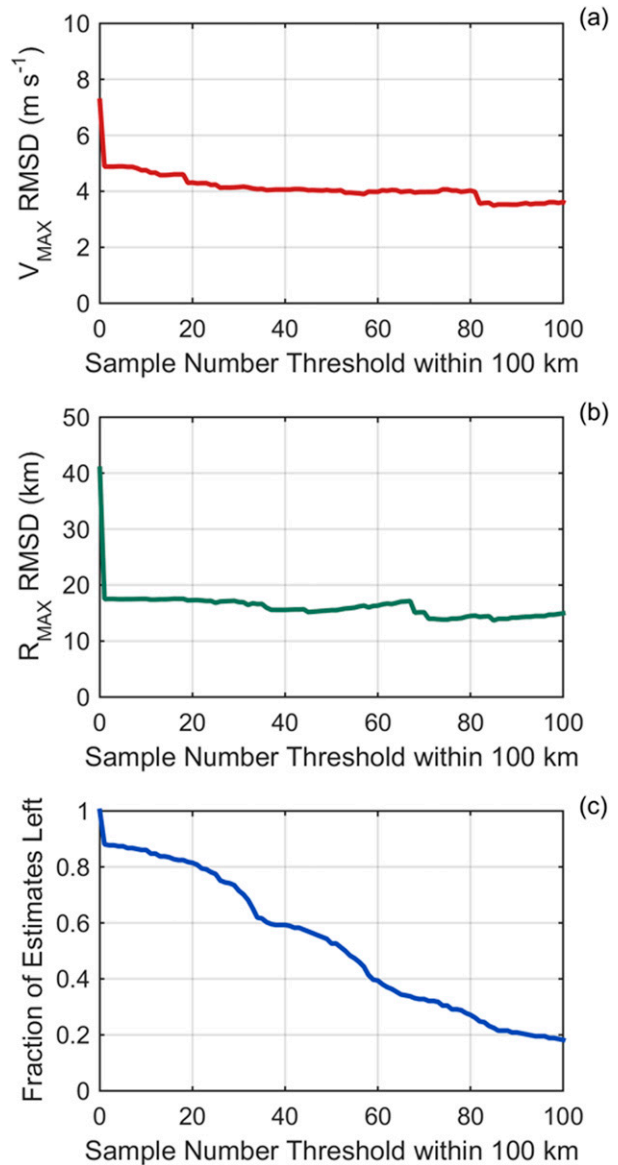


FIG. 8. (a) The RMSD between the HWRf- and CYGNSS-derived V_{MAX} depending on the QC filter threshold used. The QC keeps test cases that have a number of observations within 100 km from the storm center above the sample number threshold plotted on the x axis. (b) As in (a), but for R_{MAX} . (c) The fraction of the original test case estimates left that are used to derive the RMSD in (a) and (b).

can and will be derived from the coverage statistics in this region for the V_{MAX} and R_{MAX} metrics.

Figure 9 shows the results of a similar sensitivity experiment for the wind radii. Here, a different sampling characteristic was found to be more indicative of the performance. The number of CYGNSS samples between 100 km and R_{34} was used. As above with V_{MAX} and R_{MAX} , as the minimum threshold for the number of

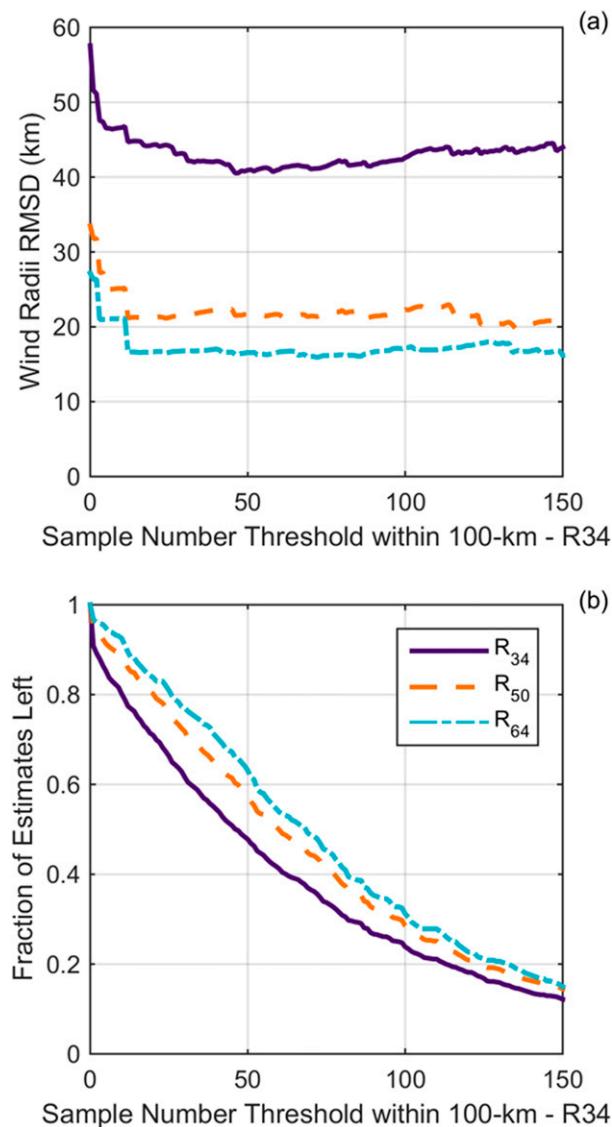


FIG. 9. (a) The RMSD between the HWRF- and CYGNSS-derived wind radii depending on the QC applied. The QC keeps test cases that have a number of observations outside 100 km from the storm center (but within the estimate of R_{34}) above the sample number threshold plotted on the x axis. (b) The fraction of the original test case estimates left that are used to derive the RMSD in (a).

samples increases, the performance of the wind radii estimates improves (see Fig. 9a). Of course, the more stringent the threshold is, the fewer cases remain (see Fig. 9b).

d. Quality-control test procedures

QC filters are derived using the results of the sensitivity experiments. The filters are intended to identify CYGNSS sampling conditions under which the TC

metric estimates are of acceptable quality. However, the filters should not be so stringent that they eliminate too large a fraction of the possible storm cases. For estimates of V_{MAX} and R_{MAX} , a sampling threshold test is used given by

$$\text{num}_{\text{obs}_{100}} \geq N, \tag{5}$$

where $\text{num}_{\text{obs}_{100}}$ is the number of observations within 100 km of the storm center for a particular storm case, and N is the filter threshold. For this study, we choose $N = 20$ as a good balance between high algorithm performance and not filtering out too many storm cases. For estimates of wind radii, a different sampling test is used given by

$$\text{num}_{\text{obs}_{100-R34}} \geq M, \tag{6}$$

where $\text{num}_{\text{obs}_{100-R34}}$ is the number of observations between 100 km of the storm center and R_{34} for a particular quadrant, and M is the filter threshold. For this study, we choose $M = 30$. Higher values produce only marginal improvement in performance while eliminating a significant fraction of the storm cases.

5. Final results

Figure 10 shows the histograms of error for all TC metrics after the QC filters described above have been applied. The original histogram data shown in Fig. 5 are included for convenience. The means and standard deviations derived from the Fig. 10 cases are listed in Table 3. Overall, the QC filters remove the egregious outliers while retaining most of the higher-quality estimates. As a result, the RMSE in the metrics is improved. Additionally, the bias in the estimates remains small after QC filters are applied.

6. Discussion

The methods presented here enable CYGNSS-based estimates of V_{MAX} , R_{MAX} , and wind radii. The estimates require a sufficient number of observations in the appropriate regions of the storm; this requirement is met using appropriate quality-control filters. For example, data availability within the inner core best predicts the quality of the inner-core metrics, namely, V_{MAX} and R_{MAX} . Wind radii estimates require sufficient sampling in an annular region outside of the inner core of the storm, between 100 km and R_{34} , and the sampling is quadrant dependent.

The results presented here assume that all eight microsatellites are available to sample the winds. If a

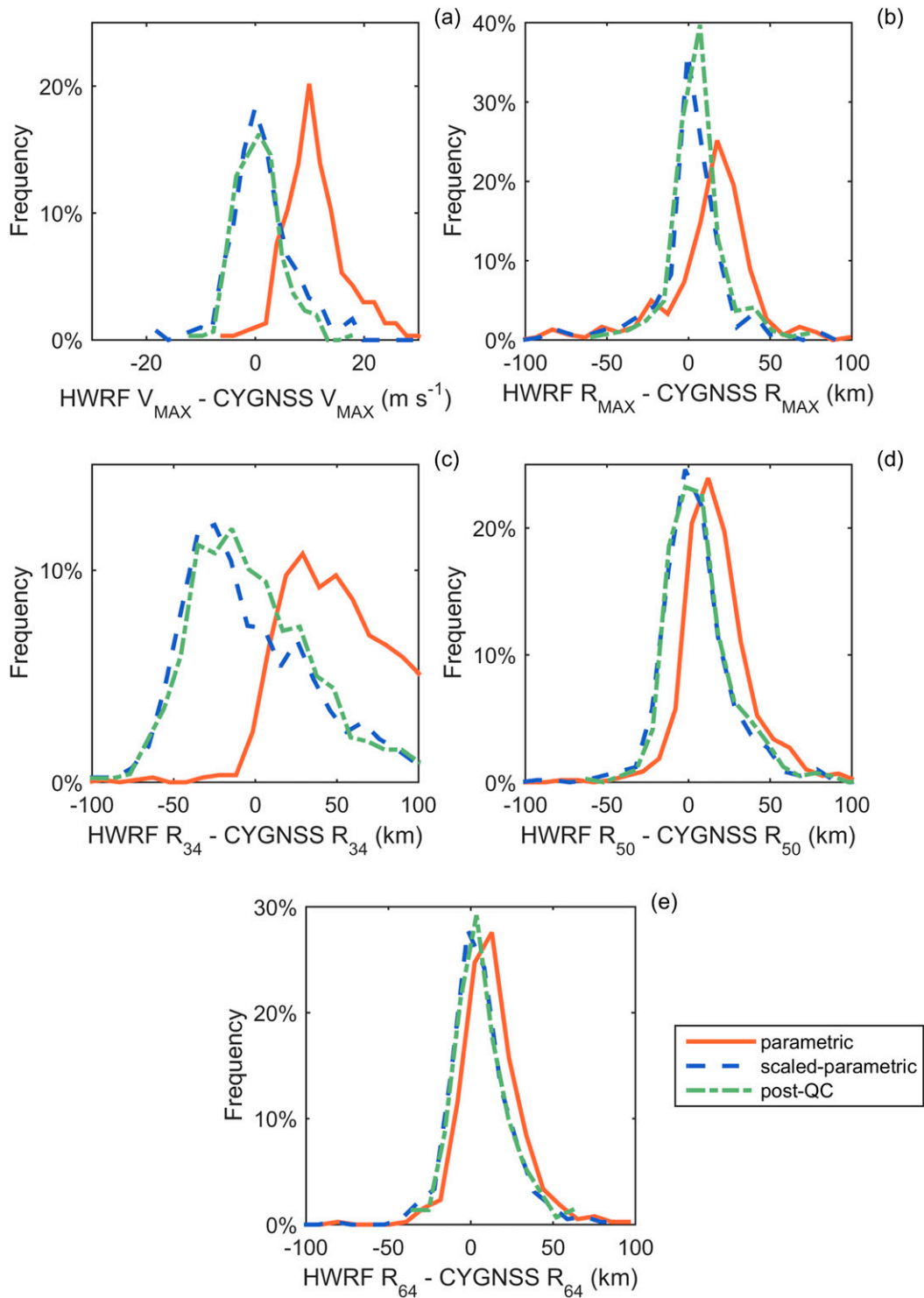


FIG. 10. Histograms of error, normalized to percentages, in all parametric, scaled-parametric, and QCed scaled-parametric metrics. Error is defined here as true – estimated.

TABLE 3. Mean and standard deviation of the error plotted in Fig. 10 for each parametric and scaled-parametric metric as well as the QCed scaled-parametric metrics.

Metric	Mean			Standard deviation		
	Parametric	Scaled parametric	Post-QC	Parametric	Scaled parametric	Post-QC
V_{MAX} ($m s^{-1}$)	10.4	0.8	-0.4	6.9	7.2	4.3
R_{MAX} (km)	1.7	-6.4	-0.04	54.0	41.7	17.4
R_{34} (km)	57.4	-5.9	-4.6	55.6	57.3	41.3
R_{50} (km)	11.9	-1.1	2.1	33.4	33.5	21.6
R_{64} (km)	5.7	-0.6	1.6	27.7	27.2	16.8

failure were to occur, the number of observations available for retrievals might be affected. To illustrate the effect of losing spacecraft (s/c), Fig. 11 shows the cumulative density function (CDF) of the number of s/c used by all test cases after the quality-control filter is applied. For example, ~81% of the test cases use six or fewer s/c to estimate V_{MAX} and R_{MAX} , and ~92% use six or fewer to estimate the wind radii. Note that wind radii estimates are more likely to have fewer s/c involved than for estimates of V_{MAX} and R_{MAX} because the wind radii estimates are quadrant limited. The decrease in the CDF when fewer s/c are available gives an indication of the impact of losing one or more of them. For example, the decrease from CDF(6 s/c) to CDF(5 s/c) describes the fraction of test cases using six s/c for which estimates would not have been possible if one s/c were lost. If the decrease from CDF(N) to CDF($N - 1$) is averaged over all $N = 2-8$, this gives an estimate of the fraction of all test cases for which estimates would not have been possible if one s/c were lost. For the CDF corresponding to V_{MAX} and R_{MAX} , the result is an average decrease by 14%. For the case of two s/c lost [i.e., a decrease from CDF(N) to CDF($N - 2$)], the average decrease is 29%, and it is 44% for a loss of three s/c. For estimates of the wind radii, the corresponding decreases are comparable. Note that these are overall statistical impacts on s/c loss, and the impact on any individual test case would require a more detailed sensitivity analysis.

Another potential factor in performance is the type and location of the storm. Figure 12 examines the impact that intensity has on the performance of the V_{MAX} and R_{MAX} estimates. Here, the test cases are separated into those that, according to HWRF, have an intensity estimate either below or above $33 m s^{-1}$ —differentiating between tropical storm and hurricane strength. Figure 12a shows that the spread in error is slightly larger in the stronger storms. Figure 12b shows that the spread in R_{MAX} error is larger for tropical storms. Both of these performance distinctions make sense considering that, in both instances, the spread is

larger for the population with larger values of the metric in question.

Figure 13 compares the performance of all TC metrics depending on the basin location of the storm. The error plotted is with QC filtering. Notably, the spread in V_{MAX} error is larger in the western Pacific test cases, which makes sense as these cases tend to have higher intensity. Another interesting takeaway from Fig. 13 is shown in Fig. 13c; here, the bias in Atlantic and eastern Pacific R_{MAX} error is more pronounced than that in the western Pacific. Basin-specific R_{MAX} performance will be examined further postlaunch with CYGNSS data in order to determine whether different scaling factors are required for different basins. In summary, assuming that these simulations are close to the true or real data fields, Figs. 12 and 13 illustrate situations where one might expect better or worse performance.

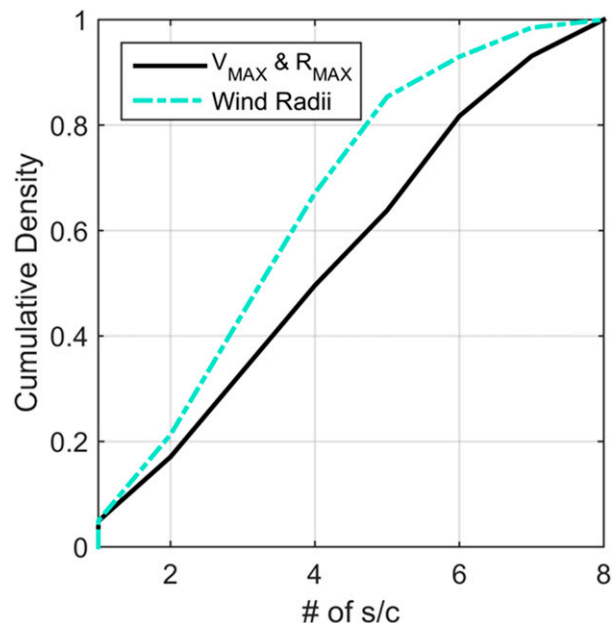


FIG. 11. Cumulative density function of number of s/c used to estimate V_{MAX} and R_{MAX} (solid black line) and wind radii (dashed blue line) for all test cases after QC has been applied.

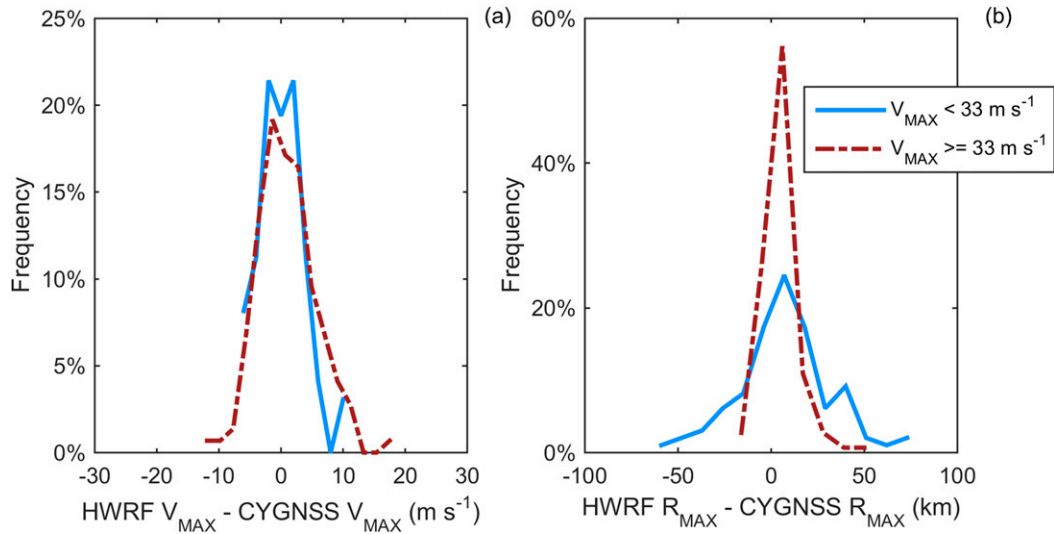


FIG. 12. Histograms, normalized to show percentages, of the QCed scaled-parametric V_{MAX} and R_{MAX} depending on the HWRf V_{MAX} threshold attained. Weaker storms ($V_{\text{MAX}} < 33 \text{ m s}^{-1}$) are plotted in solid light blue. Stronger storms ($V_{\text{MAX}} \geq 33 \text{ m s}^{-1}$) are plotted in dashed dark red.

7. Conclusions

CYGNSS will allow for a unique opportunity to estimate certain metrics of tropical cyclones that are typically quite challenging to estimate with other platforms. Since CYGNSS observations consist of collections of tracks rather than complete swaths, new estimation methods have been developed that effectively interpolate between observations in order to produce the TC metric estimates.

This study uses a mission simulator that reproduces realistic sampling patterns to be expected with CYGNSS. Sampling patterns are important to consider, as the quality of the TC metric estimates can depend strongly on them. Given good coverage, the methodology presented here enables V_{MAX} , R_{MAX} , and wind radii estimates to be made from two inputs: 1) CYGNSS observations and 2) the storm center location. Quadrant-specific inputs are used for wind radii estimates. Observations across all quadrants are used to estimate V_{MAX} and R_{MAX} . Future work includes determining if quadrant-dependent (or possibly other more complicated) methods could be used to account for asymmetries in order to improve V_{MAX} and R_{MAX} methods.

Development of the methods and applications described in this paper, as well as related areas of research (e.g., center fixing), are ongoing. Future work also includes calibration and validation of the TC metric estimates made from actual on-orbit CYGNSS data. Calibration might, for example, include retuning of the scaled-parametric relationships described in section 3d or revision of the QC filter thresholds. Validation will

follow from comparisons with coincident ground truth sources such as airborne reconnaissance underflights. If skillful, CYGNSS-based wind radii estimates could be included in the objective best-track methodology used at JTWC and NHC (Sampson et al. 2017); the small-biased CYGNSS-based method presented here—as determined from simulated observations—could be complementary to the other methods, which are typically high biased. Finally, while these methods were developed with CYGNSS in mind, it is possible that this methodology could also be applied to other types of observations, in particular those for which gaps in spatial sampling also exist.

Acknowledgments. The authors thank Chris Landsea, John Knaff, and one anonymous reviewer for their in-depth reviews and helpful suggestions that have helped to improve this paper. The authors acknowledge the hard work of several CYGNSS science team members who supported this work. The HWRf dataset was gathered by Faozi Said and Golf Seubson Soisuvann. The simulated CYGNSS observations were developed based on the work by Andrew O'Brien and Aaron Ridley. This work was supported in part by NASA Science Mission Directorate Contract NNL13AQ00C.

APPENDIX A

Summary of Storms Used

Table A1 provides a summary of all the storms used in this study.

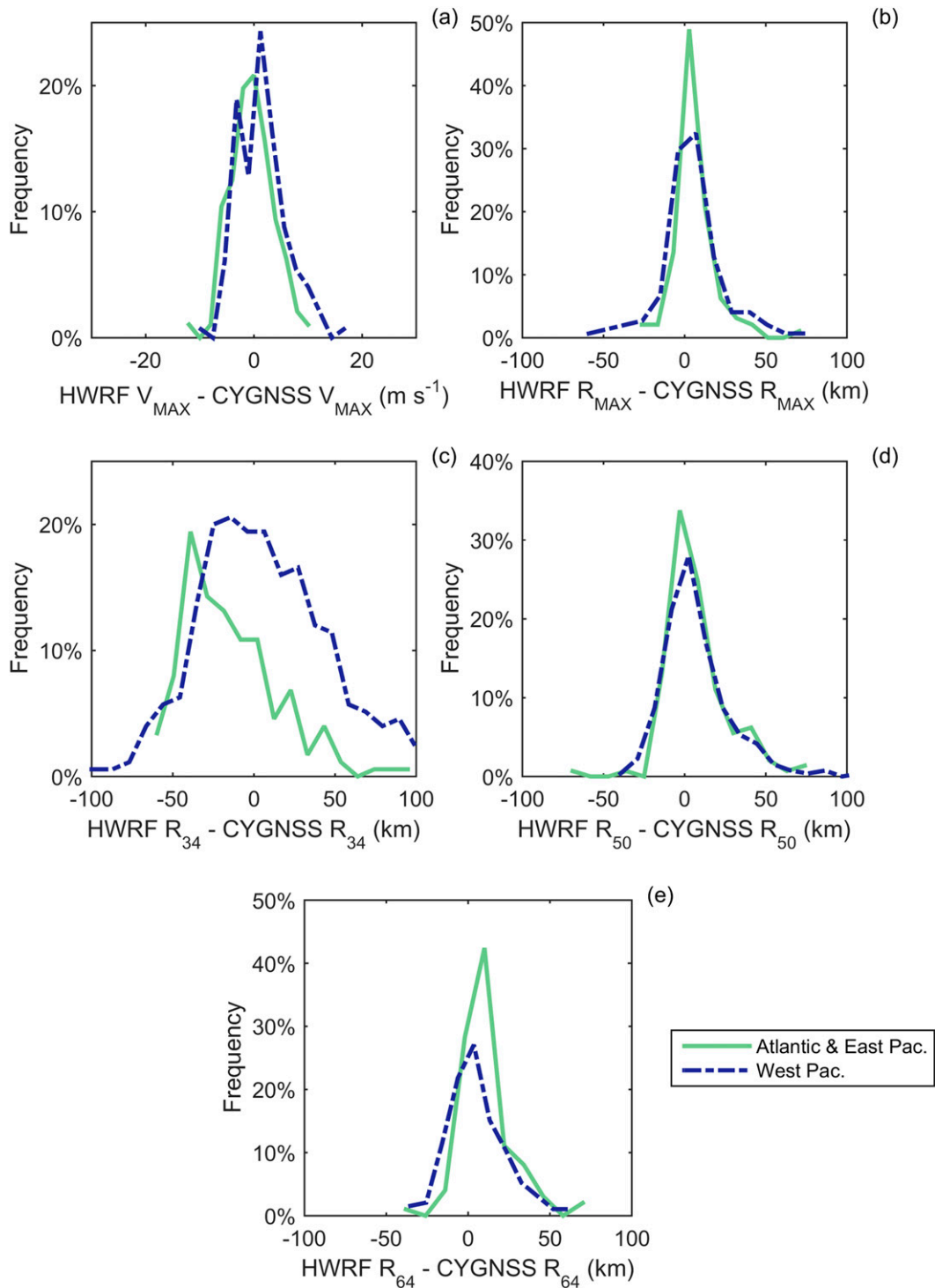


FIG. 13. Histograms, normalized to show percentages, of the QCed scaled-parametric metrics depending on the test case basin. Storms from the Atlantic and east Pacific basins are plotted in solid light green. Storms from the western Pacific basin are plotted in dashed dark blue.

TABLE A1. A summary of all of the storms used in this study, with the storm name, the number of cases for that particular storm, the maximum wind speed V_{MAX} , the storm center latitude and longitude at the point in time corresponding to the V_{MAX} case, and the year for each storm.

Storm name	No. of storm test cases	V_{MAX} ($m s^{-1}$)	Storm center lat ($^{\circ}N$)	Storm center lon ($^{\circ}E$)	Storm test case year
Danielle	11	54	26.8	300.3	2010
Estelle	4	27	17.3	250.8	2010
Frank	2	40	17.7	250.6	2010
Igor	13	66	17.6	310.7	2010
Julia	7	59	17.7	327.8	2010
Adrian	6	63	14.5	254.7	2011
Bret	1	24	29.8	284	2011
Calvin	3	36	16.7	250.9	2011
Dora	2	41	19.4	250.6	2011
Eugene	14	61	15.7	245.3	2011
Fernanda	5	28	14.7	217.3	2011
Gert	2	24	37.9	303	2011
Greg	4	36	18.5	248.6	2011
Hilary	12	59	17.1	250.6	2011
Katia	15	55	27	294.1	2011
Maria	4	33	33.7	293.1	2011
Ophelia	4	50	24	296.9	2011
Philippe	4	25	22.9	314.8	2011
Yagi	3	26	28.6	136.5	2013
Leepi	1	21	19.6	126.1	2013
Soulik	14	66	21.3	135.3	2013
Eleven	2	72	15.7	132.7	2013
Trami	2	28	19.9	128.3	2013
Man-yi	1	24	25.8	136	2013
Usagi	5	57	17.9	127.6	2013
Pabuk	12	46	29.4	139	2013
Wutip	1	27	16.4	114.1	2013
Fitow	13	47	24.5	127.3	2013
Danas	8	47	22.8	133.4	2013
Nari	1	50	15.3	114.2	2013
Francisco	20	71	17.8	137.8	2013
Lekima	12	74	19	150.9	2013
Krosa	3	31	17	127.6	2013
Tapah	3	39	14.5	147.5	2014
Eight	8	62	18.1	132.1	2014
Nine	3	47	16.6	115.4	2014
Matmo	10	45	13.5	129.3	2014
Eleven	28	72	15.7	132.7	2014
Fengshen	5	28	29.5	136.6	2014
Fifteen	2	24	13.6	130.8	2014
Kammuri	7	28	23	145.7	2014
Phanfone	11	59	20.2	137.6	2014
Vongfong	14	74	18	131.9	2014

APPENDIX B

Derivation of Solution for Parameter a in Eq. (2)

The solution for parameter a starts with Eq. (2), previously described in section 3a:

$$V(r) = \frac{2r \left(R_{m,p} V_{m,p} + \frac{1}{2} f R_{m,p}^2 \right)}{R_{m,p}^2 + ar^b} - \frac{fr}{2}. \quad (B1)$$

To solve for the parameter a , which forces the maximum value of Eq. (B1) to be equal to parameter $V_{m,p}$, the derivative of Eq. (B1) with respect to r is found given by

$$\frac{\partial V(r)}{\partial r} = \frac{2r \left(R_{m,p} V_{m,p} + \frac{1}{2} f R_{m,p}^2 \right) [R_{m,p}^2 - a(b-1)r^b]}{(R_{m,p}^2 + ar^b)^2} - \frac{fr}{2}. \quad (B2)$$

After setting $\partial V(r)/\partial r = 0$, solving for ar^b gives

$$ar^b = \frac{-c_2 \pm \sqrt{c_2^2 - 4c_1c_3}}{2c_1}, \tag{B3}$$

where, for convenience and ease of reading, we define

$$c_1 = -\frac{f}{2}, \tag{B4}$$

$$c_2 = -fR_{m,p}^2 - 2R_{m,p}V_{m,p}(b-1) - fR_{m,p}(b-1), \tag{B5}$$

and

$$c_3 = -\frac{f}{2}R_{m,p}^4 + 2R_{m,p}^3V_{m,p} + fR_{m,p}^4. \tag{B6}$$

The negative root in Eq. (B3), which we define as c_Q , gives physical results and will be used for the remainder of the solution. Next, c_Q is used to substitute in for both ar^b and r in Eq. (B1), and $V(r)$ is set equal to $V_{m,p}$, which gives a solution for a in terms of $V_{m,p}$, $R_{m,p}$, and c_Q as

$$a = \left(\frac{c_4 + c_5 + c_6 + c_7}{V_{m,p}R_{m,p}^2 + c_QV_{m,p}} \right)^b, \tag{B7}$$

where, for ease of readability, we define

$$c_4 = 2R_{m,p}V_{m,p}c_Q^{1/b}, \tag{B8}$$

$$c_5 = fR_{m,p}^2c_Q^{1/b}, \tag{B9}$$

$$c_6 = -\frac{f}{2}c_Q^{1/b}, \text{ and} \tag{B10}$$

$$c_7 = -\frac{f}{2}c_Qc_Q^{1/b}. \tag{B11}$$

APPENDIX C

Parametric Wind Model Algorithm Procedures

The parametric wind model algorithm is embedded in the outlined procedures in Fig. 2. The algorithm consists of two main parts, with the ultimate goal of solving for the three free parameters in Eq. (2): $V_{m,p}$, $R_{m,p}$, and b . To start, first guesses for $V_{m,p}$ and $R_{m,p}$ are determined, assuming $a = 1$ and $b = 2$, as the original model suggests. Second, a series of iterative steps take place in order to minimize the difference between the parametric wind model estimate of wind speed and the L2 wind speed observations. In brief, after a first guess for parameters is made, the model parameters are solved using an iterative, least squares fit of the model to the CYGNSS observations.

The iterative routine consists of a number of steps:

- 1) Calculate \mathbf{V}_{est} , which is the estimate of the radial profile of winds according to the parametric wind model, at all observation points, using the current estimate of $R_{m,p}$, $V_{m,p}$, a , and b with Eq. (2). Location is defined by \mathbf{r} , a vector of radial distances corresponding to the location of CYGNSS observations with respect to the center of the storm.
- 2) Calculate $\partial\mathbf{V} = \mathbf{V}_{est} - \mathbf{V}_{obs}$, where \mathbf{V}_{obs} is the vector consisting of the L2 surface wind speed observations collected at certain radial points defined by \mathbf{r} .
- 3) Populate the Jacobian matrix for all free parameters, defined here as

$$\mathbf{J} = \begin{bmatrix} \frac{\partial V(r_1)}{\partial V_{m,p}} & \frac{\partial V(r_1)}{\partial b} & \frac{\partial V(r_1)}{\partial R_{m,p}} \\ \vdots & \vdots & \vdots \\ \frac{\partial V(r_N)}{\partial V_{m,p}} & \frac{\partial V(r_N)}{\partial b} & \frac{\partial V(r_N)}{\partial R_{m,p}} \end{bmatrix},$$

where N is the number of CYGNSS observations, or points in \mathbf{r} . The derivatives are approximated numerically by perturbing the parametric model by small amounts, separately, for each free parameter.

- 4) Perform the generalized matrix inversion, defined as $\partial\mathbf{x} = (\mathbf{J}^T\mathbf{J} + \mathbf{R})^{-1}\mathbf{J}^T\partial\mathbf{V}$, where \mathbf{R} is a regularization matrix, used for numerical stability, defined as

$$\mathbf{R} = \gamma \begin{bmatrix} 1 & 0 & 0 \\ 0 & 1 & 0 \\ 0 & 0 & 1 \end{bmatrix},$$

with the amount of regularization dependent on the value of the relaxation parameter γ .

- 5) Update the estimate of the free parameters with

$$\mathbf{x} = \mathbf{x} + \partial\mathbf{x},$$

where the state vector \mathbf{x} is filled with the estimates of the free variables as defined by

$$\mathbf{x} = \begin{bmatrix} V_{m,p} \\ b \\ R_{m,p} \end{bmatrix},$$

with a corresponding change vector,

$$\partial\mathbf{x} = \begin{bmatrix} \partial V_{m,p} \\ \partial b \\ \partial R_{m,p} \end{bmatrix}.$$

- 6) Calculate a , with the constraint that $V_{m,p} =$ the maximum value of the parametric wind model. See details in [appendix B](#).
- 7) Update $\partial \mathbf{V} = \mathbf{V}_{est} - \mathbf{V}_{obs}$ using the latest parametric wind model estimate.
- 8) Check to make sure parameters are positive, and force them positive if necessary.
- 9) Iterate steps 1–8 until the problem has converged.

The entire iterative routine outlined above in steps 1–9 is potentially repeated as well. The population of CYGNSS observations that are used in the parametric wind model fit are the samples lying within a distance R_{Limit} of the storm center. The R_{Limit} is initially set to 200 km for North Atlantic and eastern Pacific storms and 300 km for western Pacific storms. After the first iteration, the estimate of R_{34} , given the parametric model $R_{34,P}$ is compared with R_{Limit} . If they are not sufficiently close, currently defined as being within 10 km, then R_{Limit} is set equal to $R_{34,P}$, a new population of observations is selected, and the processes outlined above are repeated. Eventually (in practice, within just a few iterations), the values of $R_{34,P}$ and R_{Limit} converge, and the parametric model estimation is complete. Results from the last iteration are used for the products.

REFERENCES

- Bessho, K., M. DeMaria, and J. A. Knaff, 2006: Tropical cyclone wind retrievals from the Advanced Microwave Sounding Unit (AMSU): Application to surface wind analysis. *J. Appl. Meteor. Climatol.*, **45**, 399–415, doi:[10.1175/JAM2352.1](#).
- Brennan, M. J., C. C. Hennon, and R. D. Knabb, 2009: The operational use of QuikSCAT ocean vector winds at the National Hurricane Center. *Wea. Forecasting*, **24**, 621–645, doi:[10.1175/2008WAF2222188.1](#).
- Chan, T. F. K., and J. C. L. Chan, 2012: Size and strength of tropical cyclones as inferred from QuikSCAT data. *Mon. Wea. Rev.*, **140**, 811–824, doi:[10.1175/MWR-D-10-05062.1](#).
- Chavas, D. R., and K. A. Emanuel, 2010: A QuikSCAT climatology of tropical cyclone size. *Geophys. Res. Lett.*, **37**, L18816, doi:[10.1029/2010GL044558](#).
- , N. Lin, and K. Emanuel, 2015: A model for the complete radial structure of the tropical cyclone wind field. Part I: Comparison with observed structure. *J. Atmos. Sci.*, **72**, 3647–3662, doi:[10.1175/JAS-D-15-0014.1](#).
- Chu, J.-H., C. R. Sampson, A. S. Levin, and E. Fukada, 2002: The Joint Typhoon Warning Center tropical cyclone best tracks 1945–2000. Joint Typhoon Warning Center Rep., 22 pp.
- Clarizia, M. P., and C. S. Ruf, 2016: Wind speed retrieval algorithm for the Cyclone Global Navigation Satellite System (CYGNSS) mission. *IEEE Trans. Geosci. Remote Sens.*, **54**, 4419–4432, doi:[10.1109/TGRS.2016.2541343](#).
- Demuth, J. L., M. DeMaria, and J. A. Knaff, 2006: Improvement of Advanced Microwave Sounding Unit tropical cyclone intensity and size estimation algorithms. *J. Appl. Meteor. Climatol.*, **45**, 1573–1581, doi:[10.1175/JAM2429.1](#).
- Dolling, K., E. Ritchie, and J. Tyo, 2016: The use of the deviation angle variance technique on geostationary satellite imagery to estimate tropical cyclone size parameters. *Wea. Forecasting*, **31**, 1625–1642, doi:[10.1175/WAF-D-16-0056.1](#).
- Dvorak, V. F., 1975: Tropical cyclone intensity analysis and forecasting from satellite imagery. *Mon. Wea. Rev.*, **103**, 420–430, doi:[10.1175/1520-0493\(1975\)103<0420:TCIAAF>2.0.CO;2](#).
- , 1984: Tropical cyclone intensity analysis using satellite data. NOAA Tech. Rep. 11, 45 pp.
- Ebuchi, N., H. C. Graber, and M. J. Caruso, 2002: Evaluation of wind vectors observed by QuikSCAT/SeaWinds using ocean buoy data. *J. Atmos. Oceanic Technol.*, **19**, 2049–2062, doi:[10.1175/1520-0426\(2002\)019<2049:EOWVOB>2.0.CO;2](#).
- Emanuel, K., and R. Rotunno, 2011: Self-stratification of tropical cyclone outflow. Part I: Implications for storm structure. *J. Atmos. Sci.*, **68**, 2236–2249, doi:[10.1175/JAS-D-10-05024.1](#).
- Fetnat, G., A. Homaifar, and K. R. Knapp, 2013: Objective tropical cyclone intensity estimation using analogs of spatial features in satellite data. *Wea. Forecasting*, **28**, 1446–1459, doi:[10.1175/WAF-D-13-00006.1](#).
- Figa-Saldana, J., J. J. W. Wilson, E. Attema, R. Gelsthorpe, M. R. Drinkwater, and A. Stoffelen, 2002: The Advanced Scatterometer (ASCAT) on the Meteorological Operational (MetOp) platform: A follow on for European wind scatterometers. *Can. J. Remote Sens.*, **28**, 404–412, doi:[10.5589/m02-035](#).
- Fore, A. G., S. H. Yueh, W. Tang, B. Stiles, and A. K. Hayashi, 2016: Combined active/passive retrievals of ocean vector wind and sea surface salinity with SMAP. *IEEE Trans. Geosci. Remote Sens.*, **54**, 7396–7404, doi:[10.1109/TGRS.2016.2601486](#).
- Harper, B. A., J. D. Kepert, and J. D. Ginger, 2010: Guidelines for converting between various wind averaging periods in tropical cyclone conditions. World Meteorological Organization Tropical Cyclone Programme Sub-Project Rep. WMO/TD-1555, 54 pp.
- Kidder, S. Q., M. D. Goldberg, R. M. Zehr, M. DeMaria, J. F. W. Purdom, C. S. Velden, N. C. Grody, and S. J. Kusselson, 2000: Satellite analysis of tropical cyclones using the Advanced Microwave Sounding Unit (AMSU). *Bull. Amer. Meteor. Soc.*, **81**, 1241–1259, doi:[10.1175/1520-0477\(2000\)081<1241:SAOTCU>2.3.CO;2](#).
- Knaff, J. A., D. P. Brown, J. Courtney, G. M. Gallina, and J. L. Beven II, 2010: An evaluation of Dvorak technique-based tropical cyclone intensity estimates. *Wea. Forecasting*, **25**, 1362–1379, doi:[10.1175/2010WAF2222375.1](#).
- , M. DeMaria, D. A. Molenar, C. R. Sampson, and M. G. Seybold, 2011: An automated, objective, multisatellite platform tropical cyclone surface wind analysis. *J. Appl. Meteor. Climatol.*, **50**, 2149–2166, doi:[10.1175/2011JAMC2673.1](#).
- , S. P. Longmore, and D. A. Molenar, 2014: An objective satellite-based tropical cyclone size climatology. *J. Climate*, **27**, 455–476, doi:[10.1175/JCLI-D-13-00096.1](#).
- , —, R. T. DeMaria, and D. A. Molenar, 2015: Improved tropical-cyclone flight-level wind estimates using routine infrared satellite reconnaissance. *J. Appl. Meteor. Climatol.*, **54**, 463–478, doi:[10.1175/JAMC-D-14-0112.1](#).
- , C. J. Slocum, K. D. Musgrave, C. R. Sampson, and B. R. Strahl, 2016: Using routinely available information to estimate tropical cyclone wind structure. *Mon. Wea. Rev.*, **144**, 1233–1247, doi:[10.1175/MWR-D-15-0267.1](#).
- Kossin, J. P., J. A. Knaff, H. I. Berger, D. C. Herndon, T. A. Cram, C. S. Velden, R. J. Murnane, and J. D. Hawkins, 2007: Estimating hurricane wind structure in the absence of aircraft reconnaissance. *Wea. Forecasting*, **22**, 89–101, doi:[10.1175/WAF985.1](#).

- Landsea, C. W., and J. L. Franklin, 2013: Atlantic hurricane database uncertainty and presentation of a new database format. *Mon. Wea. Rev.*, **141**, 3576–3592, doi:10.1175/MWR-D-12-00254.1.
- Madsen, N. M., and D. G. Long, 2016: Calibration and validation of the RapidScat scatterometer using tropical rainforests. *IEEE Trans. Geosci. Remote Sens.*, **54**, 2846–2854, doi:10.1109/TGRS.2015.2506463.
- Morris, M., and C. Ruf, 2017: Estimating tropical cyclone integrated kinetic energy with the CYGNSS satellite constellation. *J. Appl. Meteor. Climatol.*, **56**, 235–245, doi:10.1175/JAMC-D-16-0176.1.
- Mueller, K. J., M. DeMaria, J. A. Knaff, J. P. Kossin, and T. H. Vonder Haar, 2006: Objective estimation of tropical cyclone wind structure from infrared satellite data. *Wea. Forecasting*, **21**, 990–1005, doi:10.1175/WAF955.1.
- O'Brien, A., 2014: CYGNSS end-to-end simulator. CYGNSS Project Doc. 148-0123, 23 pp. [Available online at http://clasp-research.engin.umich.edu/missions/cygnss/reference/148-0123_CYGNSS_E2ES_EM.pdf.]
- Office of the Federal Coordinator for Meteorological Services and Supporting Research, 2017: National hurricane operations plan. National Atmospheric and Oceanic Administration Rep. FCM-P12-2017, 185 pp. [Available online at <http://www.ofcm.gov/publications/nhop/FCM-P12-2017.pdf>.]
- Olander, T. L., and C. S. Velden, 2007: The advanced Dvorak technique: Continued development of an objective scheme to estimate tropical cyclone intensity using geostationary infrared satellite imagery. *Wea. Forecasting*, **22**, 287–298, doi:10.1175/WAF975.1.
- Piñeros, M. F., E. A. Ritchie, and J. S. Tyo, 2008: Objective measures of tropical cyclone structure and intensity change from remotely sensed infrared image data. *IEEE Trans. Geosci. Remote Sens.*, **46**, 3574–3580, doi:10.1109/TGRS.2008.2000819.
- , —, and —, 2011: Estimating tropical cyclone intensity from infrared image data. *Wea. Forecasting*, **26**, 690–698, doi:10.1175/WAF-D-10-05062.1.
- Rappaport, E. N., and Coauthors, 2009: Advances and challenges at the National Hurricane Center. *Wea. Forecasting*, **24**, 395–419, doi:10.1175/2008WAF2222128.1.
- Reul, N., J. Tenerelli, B. Chapron, D. Vandemark, Y. Quilfen, and Y. Kerr, 2012: SMOS satellite L-band radiometer: A new capability for ocean surface remote sensing in hurricanes. *J. Geophys. Res.*, **117**, C02006, doi:10.1029/2011JC007474.
- , B. Chapron, E. Zabolotskikh, C. Donlon, Y. Quilfen, S. Guimbard, and J-F. Piolle, 2016: A revised L-band radiobrightness sensitivity to extreme winds under tropical cyclones: The five year SMOS-Storm database. *Remote Sens. Environ.*, **180**, 274–291, doi:10.1016/j.rse.2016.03.011.
- Ruf, C., and Coauthors, 2016: New ocean winds satellite mission to probe hurricanes and tropical convection. *Bull. Amer. Meteor. Soc.*, **97**, 385–395, doi:10.1175/BAMS-D-14-00218.1.
- Sampson, C. R., J. Hansen, P. Wittmann, J. Knaff, and A. Schumacher, 2016: Wave probabilities consistent with official tropical cyclone forecasts. *Wea. Forecasting*, **31**, 2035–2045, doi:10.1175/WAF-D-15-0093.1.
- , E. M. Fukada, J. A. Knaff, B. R. Strahl, M. J. Brennan, and T. Marchok, 2017: Tropical cyclone gale wind radii estimates for the western North Pacific. *Wea. Forecasting*, **32**, 1029–1040, doi:10.1175/WAF-D-16-0196.1.
- Tallapragada, V., and Coauthors, 2013: Hurricane Weather Research and Forecasting (HWRF) Model: 2013 scientific documentation. Development Testbed Center Rep., 99 pp. [Available online at http://www.dtcenter.org/HurrWRF/users/docs/scientific_documents/HWRFv3.5a_ScientificDoc.pdf.]
- Torn, R. D., and C. Snyder, 2012: Uncertainty of tropical cyclone best-track information. *Wea. Forecasting*, **27**, 715–729, doi:10.1175/WAF-D-11-00085.1.
- Vecchi, G., and T. Knutson, 2011: Estimating annual numbers of Atlantic hurricanes missing from the HURDAT database (1878–1965) using ship track density. *J. Climate*, **24**, 1736–1746, doi:10.1175/2010JCLI3810.1.
- Velden, C. S., T. Olander, and R. M. Zehr, 1998: Development of an objective scheme to estimate tropical cyclone intensity from digital geostationary satellite imagery. *Wea. Forecasting*, **13**, 172–186, doi:10.1175/1520-0434(1998)013<0172:DOAOST>2.0.CO;2.
- , and Coauthors, 2006: The Dvorak tropical cyclone intensity estimation technique. *Bull. Amer. Meteor. Soc.*, **87**, 1195–1210, doi:10.1175/BAMS-87-9-1195.
- Wimmers, A. J., and C. S. Velden, 2010: Objectively determining the rotational center of tropical cyclones in passive microwave satellite imagery. *J. Appl. Meteor. Climatol.*, **49**, 2013–2034, doi:10.1175/2010JAMC2490.1.
- Yueh, S. H., A. G. Fore, W. Tang, A. Hayashi, B. Stiles, N. Reul, Y. Weng, and F. Zhang, 2016: SMAP L-band passive microwave observations of ocean surface wind during severe storms. *IEEE Trans. Geosci. Remote Sens.*, **54**, 7339–7350, doi:10.1109/TGRS.2016.2600239.